Relationship between microstructure and mechanical properties of as-extruded and peak-aged Mg–6Al–3Sn–2Zn alloys

Sen WANG, Bin-jiang LV, Tie-wei XU, Ning CUI, Feng GUO

School of Mechanical and Automotive Engineering, Qingdao University of Technology, Qingdao 266525, China

Abstract: The microstructure and mechanical properties of as-extruded and as-aged Mg–6Al–3Sn–2Zn (ATZ632) alloys were investigated. The as-extruded alloy shows excellent mechanical properties, achieving the yield strength (YS), ultimate tensile strength (UTS), and elongation (EL) of 216.4 MPa, 344.3 MPa, and 18.4%, respectively. After aging treatment, the volume fraction of the precipitated $Mg_{17}Al_{12}$ phase increases and the Mg_4Zn_7 phase appears. The YS and UTS of the as-aged ATZ632 alloy increased to 252.5 and 416.2 MPa, respectively; however, the EL decreased to 10.1%. The high strength of the as-aged alloys is attributed to the precipitated Mg_4Zn_7 phase with an orientation perpendicular to the (0001) plane of α-Mg and the $Mg_{17}Al_{12}$ phase with an orientation parallel to the basal plane. Furthermore, the precipitation after aging decreases the EL. Static recrystallization grains appear during low-temperature aging at 150 °C, and their orientation shows a high degree of consistency with the c-axis perpendicular to the extrusion direction.

Key words: microstructure; mechanical properties; aging; strengthening mechanism; static recrystallization

1 Introduction

As the lightest structural materials, Mg alloys exhibit high specific strength, specific rigidity, thermal conductivity, and good electromagnetic shielding performance. Thus, they have received considerable attention in the fields of transportation and electronics [1−3]. However, the low yield strength (YS) and ultimate tensile strength (UTS) of Mg alloys limit their industrial applications. These shortcomings of cast alloys can be addressed by wrought Mg alloys, which show refined grains due to plastic deformation, thus considerably improving the mechanical properties of Mg alloys [4−7].

To further enhance the mechanical properties of Mg alloys, they are subjected to alloying, heat treatment, and plastic deformation processing [8−11]. Aging induces precipitation enhancement and grain refinement in Mg alloys, thus improving their mechanical properties. $Mg_{17}Al_{12}$, Mg_2Sn, and Mg−Zn phases are the three important precipitates during aging. LI et al [12] performed T4 (420 °C, 2 h) and double-aging treatments on an as-extruded ZM51 alloy, achieving the YS and UTS of 297 and 349 MPa, respectively, which were 65% and 22% higher than those achieved in the extruded state. The increase in the strengths was attributed to the massive precipitation of the $MgZn_2$ phase after aging, which plays an important role in the precipitation strengthening. JUNG et al [13] examined the effect of adding Sn during aging on the mechanical properties of the AZ91 alloy, reporting the precipitation of numerous Mg_2Sn phases after aging, which increased the YS of the alloy from 119.4 to 161.9 MPa.

Recently, because of their good age-hardening ability and mechanical properties, Mg−Al−Sn−Zn

alloys have garnered considerable research attention. JUNG et al [13] have detected dense continuous precipitates in the matrix of an as-aged ATZ915 alloy, which increased the hardness of the peak-aged alloy to HV 117.14 and the YS by 35.6%. The formation of the continuous precipitation phase was attributed to the presence of Sn, which can suppress the discontinuous precipitation phase and increase the density of the continuous precipitation phase during aging [14]. WU et al [15] examined an as-extruded ATZ822 alloy, which exhibited the YS, UTS, and elongation (EL) of 258 MPa, 357 MPa, and 8.76%, respectively, attributed to the presence of numerous Mg_2Sn phases and the discontinuous $Mg_{17}Al_{12}$ phase. After aging, multiple continuous and discontinuous $Mg_{17}Al_{12}$ phases precipitated in the matrix, which increased the YS and UTS of the alloy by 12.7% and 7.8%, respectively; however, EL decreased by 6.44%.

Although many studies have been conducted using Mg−Al−Sn−Zn alloys, most focus on their precipitation strengthening and mechanical properties. The influence of relatively low-temperature aging treatment on the microstructural evolution, orientation relation of Mg−Al and Mg−Zn precipitates, and mechanical properties of wrought Mg−Al−Sn−Zn alloys have not been studied. In this study, a new wrought Mg alloy was designed, and the microstructure, mechanical properties, and textural evolution of the as-extruded and as-aged Mg−6Al−3Sn−2Zn (ATZ632) alloys were examined.

2 Experimental

Pure Mg (99.8 wt.%), Al (99.9 wt.%), Sn (99.97 wt.%), and Zn (99.97 wt.%) were added in a stainless steel crucible preheated to 750 °C under the protection of a mixed gas of CO_2 (99 vol.%) and SF_6 (1 vol.%). Then, the ingot was cast at a final temperature of 720 °C using a water-cooled semi-continuous casting system with a diameter and a length of 95 and 400 mm, respectively. The chemical compositions of the ingot were evaluated using an X-ray fluorescence spectrometer (XRF− 1800 CCDE) (Table 1). The ingot was homogenized at 400 °C for 24 h in a (5 kW) heat treatment furnace, followed by quenching using water (T5). Then, extrusion was performed on a 500T forward extruder with the extrusion ratio, temperature, and

speed of 26, 300 °C, and 5 mm/s, respectively. After extrusion, the samples were subjected to aging at 150 °C.

The samples were cut perpendicularly to the extrusion direction (ED), polished, and etched in a solution containing 1 g picric acid, 5 mL glacial acetic acid, 5 mL water, and 25 mL alcohol for 5 s. The microstructure of the samples was characterized using electron scanning micro-scopy (SEM; ZEISS MERLIN Compact) with energy dispersive X-ray spectroscopy (EDS) and transmission electron microscopy (TEM; FEI Tecnai G2 F20) at 300 kV. X-ray diffraction (XRD; X′Pert PRO MRD/XL) was performed to analyze the phases of the as-extruded and as-aged samples, which were polished using a ACII polishing solution; the polishing voltage and current were 20 V and 0.14 A, respectively. Electron backscatter diffraction (EBSD) test was performed on a Hitachi S−3400N instrument at a step length of 0.5 μm, and the CHANNEL 5 software was used to analyze the EBSD data. The hardness of the samples with different aging treatment time was evaluated using an HVG−1000M automatic microhardness tester with a load of 0.49 N (50 g); each sample took 15 points to achieve the average value for data accuracy. Peak-aged and unaged as-extruded rods were also considered, and they were processed into tensile samples with a diameter and a length of 10 and 110 mm, respectively. The tensile direction (TD) was parallel to the ED. A tensile experiment was performed on a CMT−5105 stretching machine at a speed of 0.3 mm/min at room temperature. The average size and density of the precipitated phases were obtained using TEM morphological images based on the Image-Pro Plus software.

Table 1 Chemical composition of Mg−6Al−3Sn−2Zn alloy (wt.%)

Al	Sn	Zn	Mg
5.95	3.11	2.14	Bal.

3 Results

3.1 Microstructure of as-homogenized alloys

Figure 1 shows the microstructure and EDS results of the as-homogenized ATZ632 alloy. Some second phases are distributed at the grain boundary and interior of the ATZ632 alloy after homogenization (Fig. 1(a)). Based on the EDS

results (Figs. 1(b, c)), the long-strip phase contains Mg, Sn, and Zn, whereas the spherical phase contains Mg and Sn. The average grain size of the as-homogenized ATZ632 alloy is (187.4±32) μm.
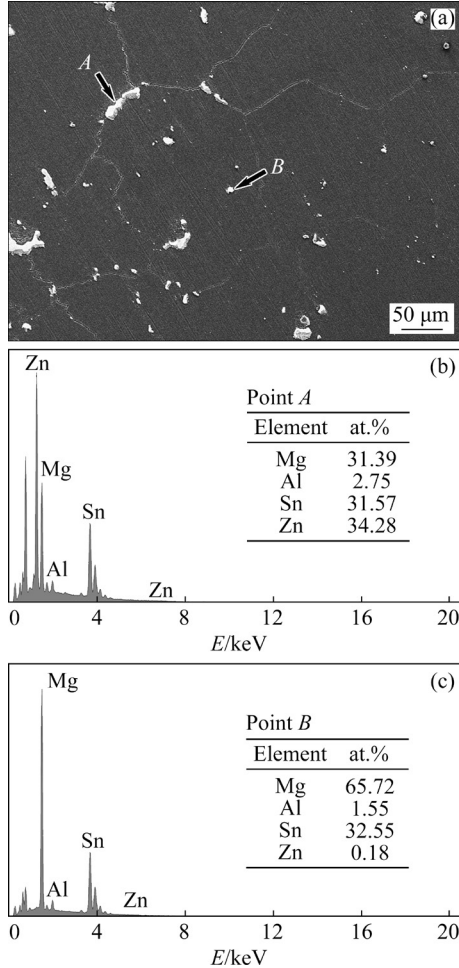

Fig. 1 Microstructure of as-homogenized ATZ632 alloy: (a) SEM image; (b, c) EDS results

3.2 Microstructure of as-extruded alloy

The grain size of the ATZ632 alloy decreases after extrusion, indicating the occurrence of dynamic recrystallization (DRX) during extrusion. The distribution of several rod-like and spherical phases is observed at the boundaries and interior of the grains (Fig. 2(a)). As shown in Figs. 2(b, c), the chemical elements of the second phase are analyzed using EDS. The rod-like phase contains Mg and Al, whereas the bright white spherical phase contains Mg and Sn. Figure 3(a) shows the inverse pole figure (IPF) of the as-extruded ATZ632 alloy. The grains are relatively uniform, and the average grain size is 15.49 μm (Fig. 3(b)). Based on the (0001) pole figure (PF) (Fig. 3(c)), the as-extruded Mg alloy shows a typical basal fiber texture. The

maximum intensity of the basal fiber texture is 9.79 MRD (i.e., multiples of random distribution). Based on the IPF in Fig. 3(d), the high-intensity component is distributed near $\langle 10\bar{1}0 \rangle$, spreads toward $\langle 0001 \rangle$ (along with a gradual weakening), and then disappears at $\langle 20\bar{2}1 \rangle$. The highest intensity point is near $\langle 10\bar{1}0 \rangle$ along the ED; therefore, the prismatic plane of most grains in the as-extruded alloy is perpendicular to the ED.
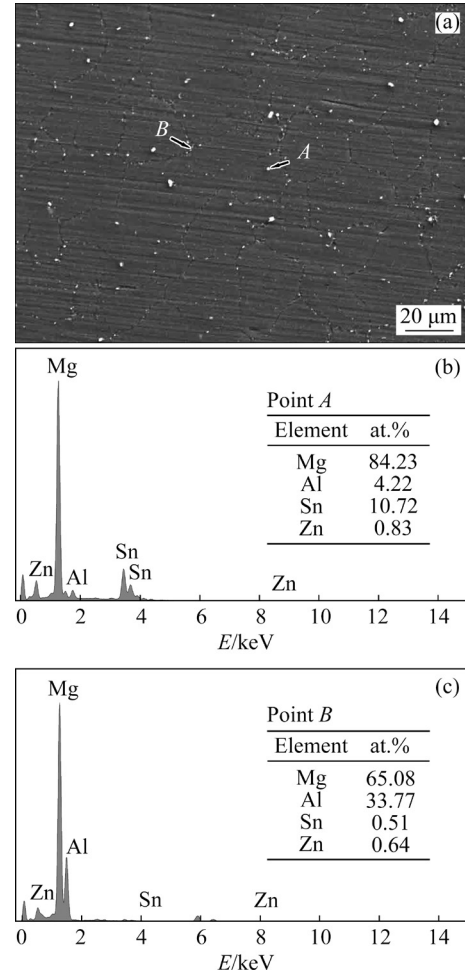

Fig. 2 Microstructure of as-extruded alloy: (a) SEM image; (b, c) EDS results

TEM analyses were conducted to identify the second phases of the as-extruded ATZ632 alloy (Fig. 4). We observed two types of precipitates (Fig. 4(a)): black irregular rod-like phase with a length and a width of ~395 and 119.5 nm, respectively (marked with *A*), and spherical phase with diameters of 50−152.6 nm (marked with *B*). The upper right corner of Fig. 4(a) shows the selected area electron diffraction (SAED) pattern of the α-Mg matrix with the zone axis $[\bar{2}4\bar{2}3]$. Based on the SAED results (Fig. 4(b)), the second phase
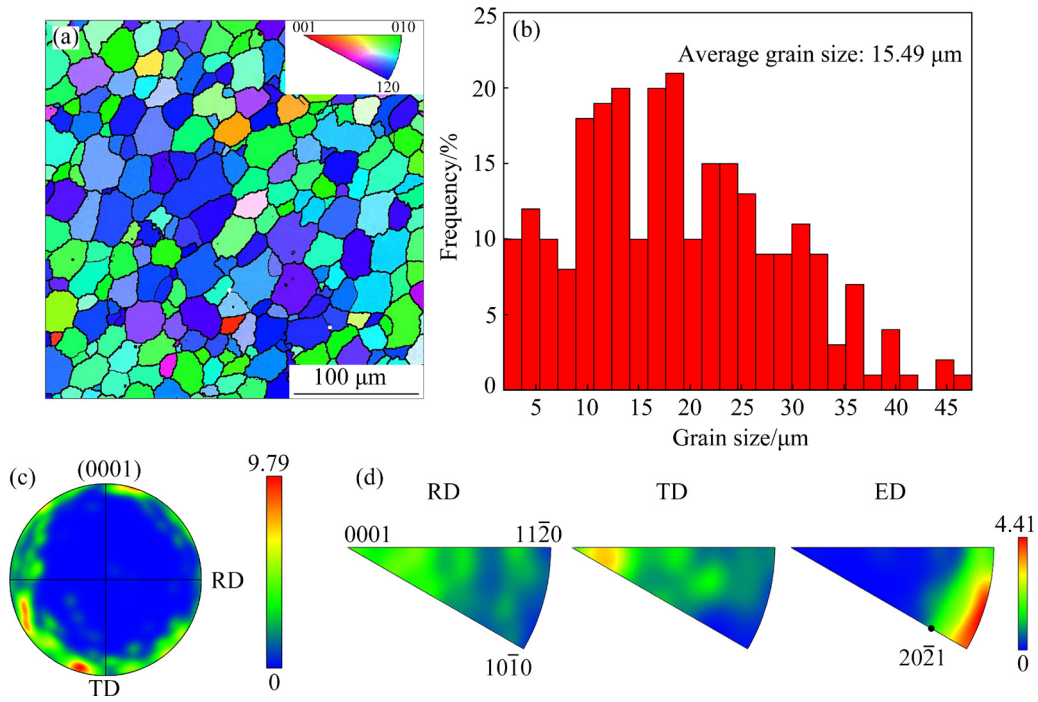
Fig. 3 Textural information of as-extruded alloy: (a) Inverse pole figure; (b) Grain size distribution map; (c) Pole figure; (d) Inverse pole figure
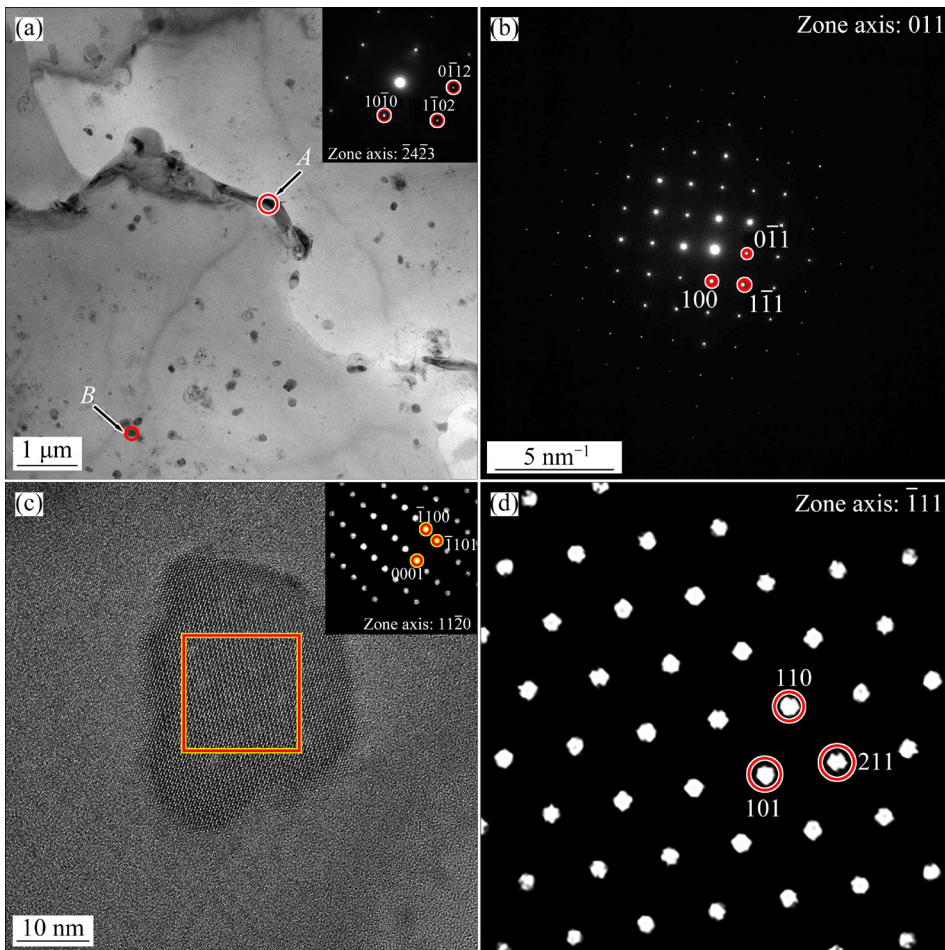

Fig. 4 Bright-field TEM image of as-extruded ATZ632 alloy (a), selected area electron diffraction (SADE) pattern of Phase *A* (b), HRTEM image of Phase *B* (c), and FFT pattern obtained from Phase *B* (d)

particle marked with A is determined to be the $Mg_{17}Al_{12}$ phase. Both $Mg_{17}Al_{12}$ and α-Mg matrix exhibit the following orientation relation: $(1\bar{1}02)_{Mg}//(1\bar{1}1)_{Mg_{17}Al_{12}}$ and $[\bar{2}4\bar{2}3]_{Mg}//[011]_{Mg_{17}Al_{12}}$. Figure 4(c) shows the high-resolution TEM image of the Phase B along the $[11\bar{2}0]_{\alpha\text{-Mg}}$ zone axis. Figure 4(d) shows the corresponding fast Fourier transformation (FFT) in Fig. 4(c) (indicated by a solid red line). The spherical phase is determined to be the Mg_2Sn phase ($a=0.674$ nm; space group $\bar{F}m3m$ [16]), exhibiting the following orientation relation: $(\bar{1}100)_{Mg}//(110)_{Mg_2Sn}$ and $[11\bar{2}0]_{Mg}//[\bar{1}11]_{Mg_2Sn}$. During extrusion, the Mg_2Sn phase can limit the movement of grain boundaries and the growth of recrystallized grains [17]. Thus, the grain size is refined after extrusion.

3.3 Aging behavior

The as-extruded ATZ632 alloy was aged for different time at 150 °C, and the obtained microhardness is shown in Fig. 5. The hardness value increases with an increase in the aging treatment time in the early stage and then decreases after reaching a peak. In the initial aging stage, the hardness of the alloy increases rapidly. After aging for 24 h, the hardness of the peak aging reaches HV 86.2, 31.4% higher than HV 65.6 obtained for the as-extruded sample, which was not subjected to aging.
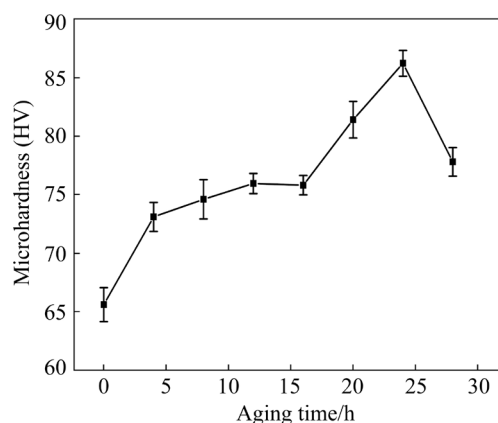
After aging, the volume fraction of precipitates

Fig. 5 Variations in Vickers hardness of ATZ632 alloy as function of aging time at 150 °C

increases (Fig. 6(a)). Many small strips and spherical phases are distributed in the discontinuous precipitation zone, and many spherical phases are uniformly distributed in the grain (Fig. 6(b)). Figures 6(c) and (d) show the EDS results. The fine strip and spherical phase particles may correspond to the $Mg_{17}Al_{12}$ and Mg_2Sn phases, respectively. The fine $Mg_{17}Al_{12}$ and Mg_2Sn precipitates show diameters of ~0.9 and 0.1 μm, respectively. The increase in the number of fine precipitates after aging is crucial in dispersion strengthening, enhancing the hardness of the alloy after aging.

The IPF of the peak-aged and as-extruded alloy (Fig. 7(a)) reveals the appearance of multiple fine grains; moreover, the grain size decreases to
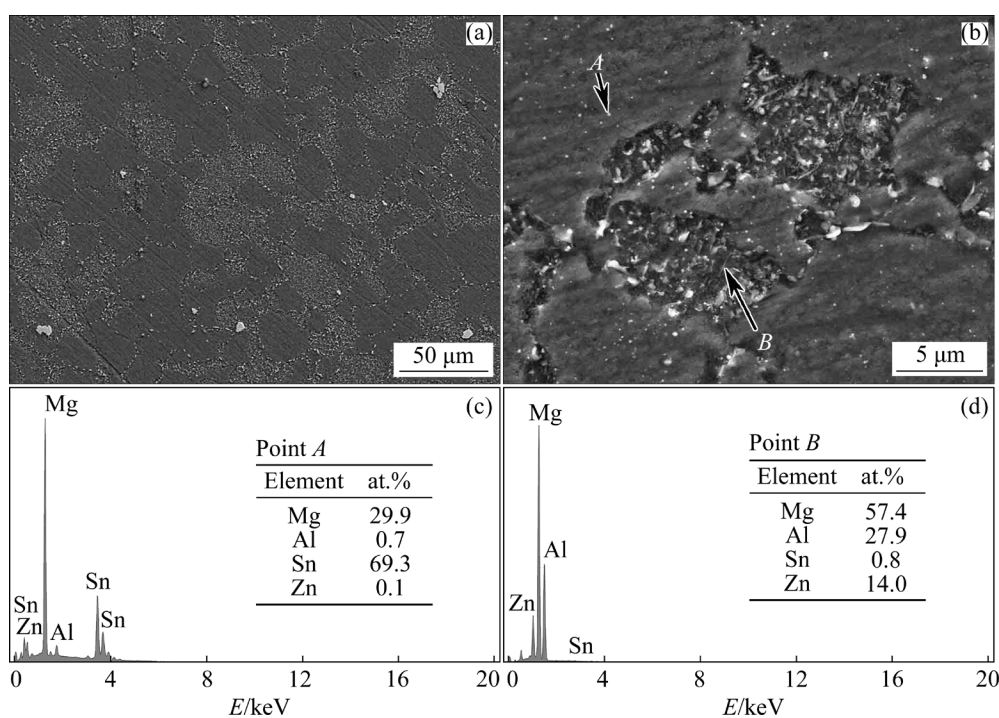

Fig. 6 Microstructures of peak-aged ATZ632 alloy: (a, b) SEM images; (c, d) EDS results
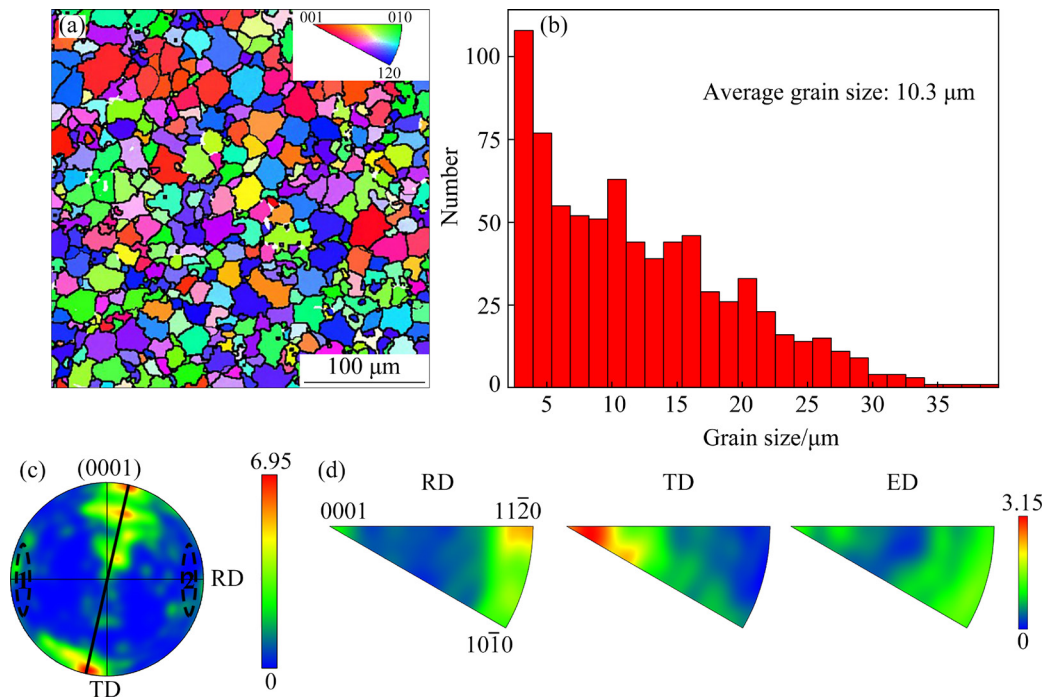
Fig. 7 Textural information of peak-aged ATZ632 alloy: (a) Inverse pole figure; (b) Grain size distribution map; (c) Pole figure; (d) Inverse pole figure

10.3 μm. Compared with the unaged as-extruded sample (Fig. 3(a)), the number of small grains increases, with ~46.6% of grains showing a grain size of <10 μm (Fig. 7(b)). Based on Fig. 7(c), the (0001) texture is observed to weaken after peak aging and the MRD decreases from 9.79 (for the unaged as-extruded alloy) to 6.95. For the as-extruded alloys, certain grains (regions indicated as 1 and 2 in Fig. 7(c)) rotate toward the TD after aging; the rotation angle is ~10° based on the (0001) PF of the unaged as-extruded alloys (Fig. 3(c)). After aging, the intensity distribution in the IPF (Fig. 7(d)) parallel to the ED is relatively uniform and no high-intensity point is observed; rather, it transfers to the IPF along the TD and RD. The highest intensity distribution is observed at the $\langle 0001 \rangle$ pole along the TD and spreads by 18° at the $\langle 10\bar{1}0 \rangle$ pole; further, there is a $\langle 10\bar{1}2 \rangle$ pole with a slightly weak intensity. The $\langle 11\bar{2}0 \rangle$ pole is another weak-intensity pole along the RD, which weakens along the arc at the $\langle 10\bar{1}0 \rangle$ pole, indicating that most prismatic planes of the grains are perpendicular to the ED after aging. However, a small portion of the grains rotate by 30° or 70° around the *c*-axis, thus making the pyramidal plane parallel to the RD.

Figure 8 shows the XRD patterns of the as-extruded ATZ632 alloy at aging treatment time of 0 and 24 h. The as-extruded alloy contains α-Mg, Mg_2Sn, and $Mg_{17}Al_{12}$ phases. A new diffraction peak is detected at 2θ of 36° after 24 h of aging, indicating additional $Mg_{17}Al_{12}$ precipitates (Fig. 8(b)). Zn precipitates from the matrix after aging [18,19] and a new Mg_4Zn_7 phase appear; however, the Mg_4Zn_7 phase is not detected in the aging state (Fig. 8(b)). This may be attributed to the low Zn content because less Mg_4Zn_7 phase precipitates and is not detected.
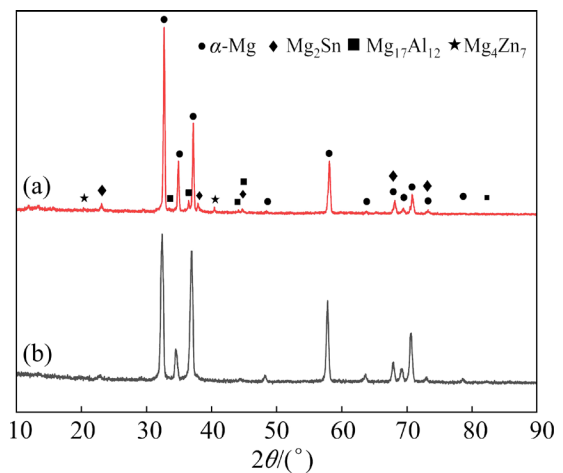

Fig. 8 XRD patterns of ATZ632 alloy before aging (a) and after being aged at 150 °C for 24 h (b)

In Fig. 9(a), three phases are observed: spherical phase (marked with A), lamellar phase (marked with B), and rod-like phase (marked with C). This shows that a new phase precipitates from the matrix after 24 h of aging. Phase A is reported to be Mg_2Sn based on SAED results (Fig. 9(b)). The diameter of Mg_2Sn, which is larger than that of the as-extruded sample, is between 80.9 and 236.8 nm. The upper right corner of Fig. 9(c) shows the diffraction pattern of the α-Mg matrix along the zone axis $[1\bar{2}10]$. As shown in Fig. 9(d), the diffraction pattern of Phase B, which is reported to be the $Mg_{17}Al_{12}$ phase, shows the following orientation relation with the matrix: $(0\bar{1}1)_{Mg_{17}Al_{12}}$ // $(0001)_{Mg}$ and $[111]_{Mg_{17}Al_{12}}$//$[1\bar{2}10]_{Mg}$. Morphology of $Mg_{17}Al_{12}$ changes from an irregular rod-like phase during extrusion to a regularly arranged lamellar phase along the $[\bar{1}010]$ direction parallel to the matrix (Fig. 9(a)); it precipitates from the basal plane of α-Mg [20]. Both the length and width of the $Mg_{17}Al_{12}$ precipitates are ~86.77 and 37.00 nm, respectively. The volume fraction
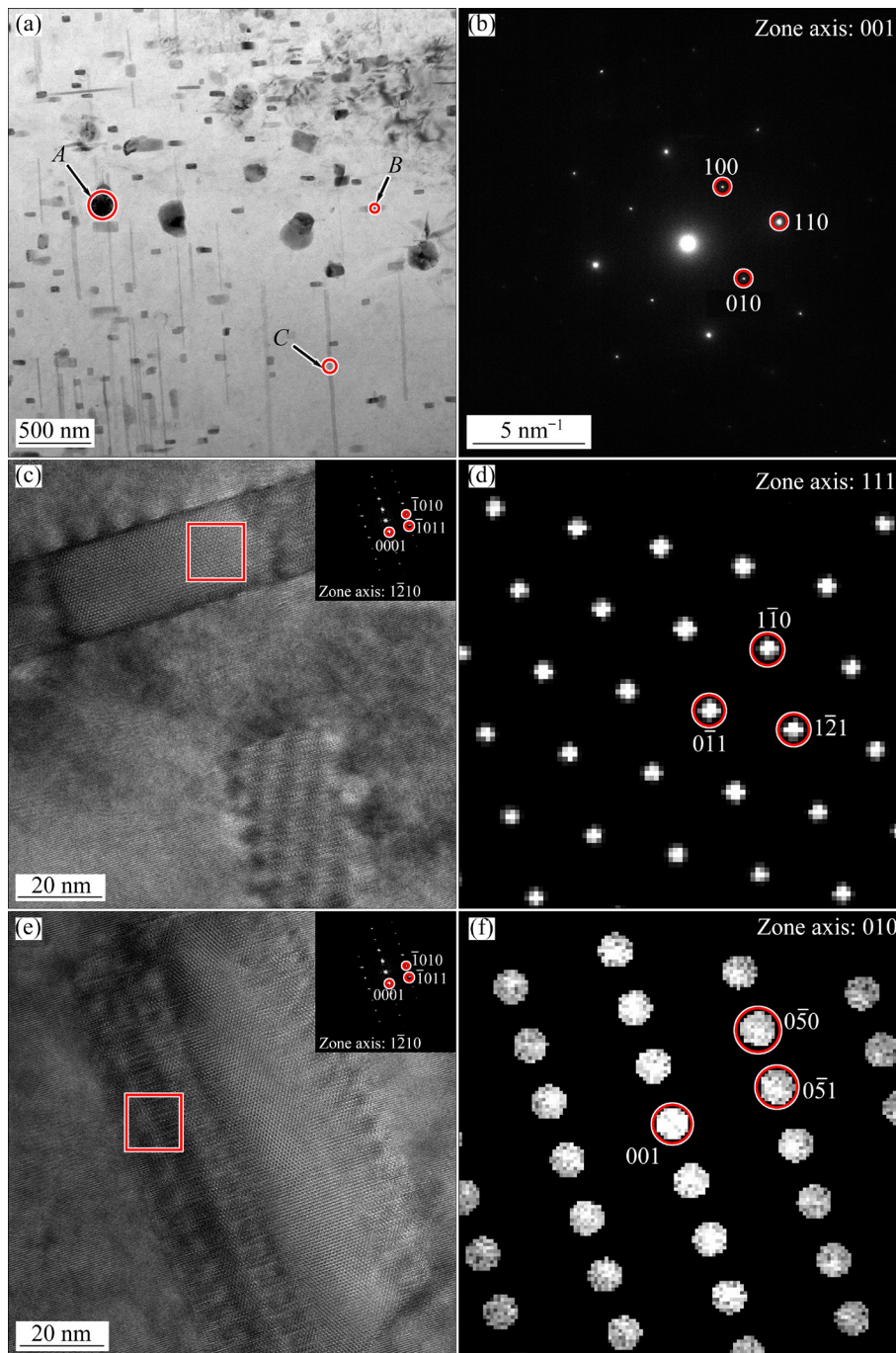

Fig. 9 Bright-field TEM image of peak-aged ATZ632 alloy (a), SAED pattern of Phase A (b), HRTEM image of Phase B (c), FFT pattern obtained from Phase B (d), HRTEM image of Phase C (e), and FFT pattern obtained from Phase C (f)

increases to 2.85%. Figure 9(e) shows the HRTEM image of Phase C, where the zone axis of the α-Mg matrix is $[1\bar{2}10]$. The rod-like phase is parallel to the [0001] direction of the matrix, and it precipitates from the prismatic plane of α-Mg with the length and width of 613.9 and 30.0 nm, respectively. The rod-like phase is reported to be Mg_4Zn_7 based on the diffraction pattern in Fig. 9(f), consistent with the previous report [21]; furthermore, the orientation relation with α-Mg is $(001)_{Mg_4Zn_7}//(0001)_{Mg}$ and $[010]_{Mg_4Zn_7}//[1\bar{2}10]_{Mg}$.

3.4 Mechanical properties

Figure 10 shows the mechanical properties of the as-extruded and as-aged ATZ632 alloys. The YS and UTS of the ATZ632 alloy after 24 h of aging are 252.5 and 416.2 MPa, respectively, 16.47% and 20.82% higher than those of the as-extruded alloy, respectively. However, the EL decreases from 18.4% to 10.1%.
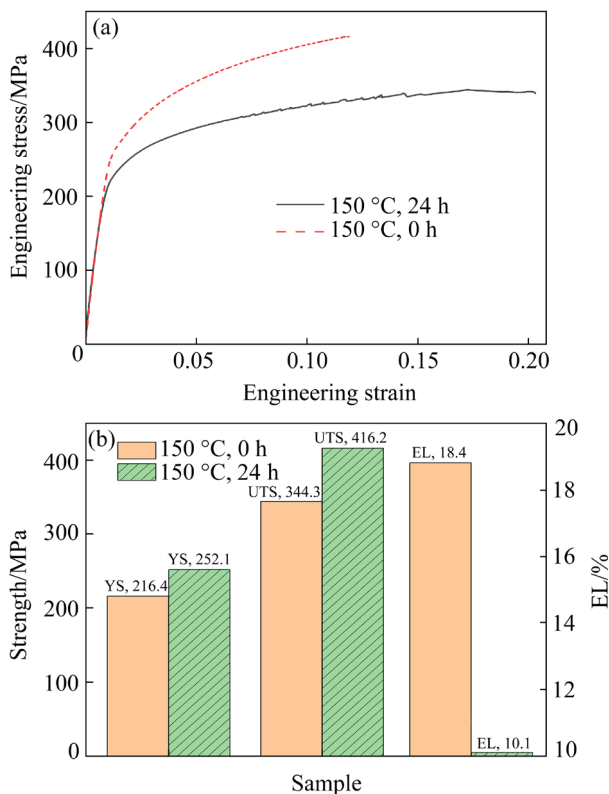

Fig. 10 Mechanical properties of as-extruded and peak-aged ATZ632 alloy

4 Discussion

4.1 Influence of aging on microstructure

The grain size is refined after aging at 150 °C, which may be attributed to the static

recrystallization (SR) caused by aging [22]. The static recrystallized grains are formed at the original grain boundaries (Fig. 7(a)). Because of the high dislocation density, high storage energy, and stress concentration at the grain boundaries [23−26], the static recrystallized grains nucleate in the as-extruded ATZ632 alloy during aging. The high annealing temperature provides sufficient energy for the growth of static recrystallized grains and affords high static recrystallized volume fractions of 40%−70%. Herein, limited energy is available for the growth of the recrystallized grains because of the relatively low aging temperature of 150 °C. During aging, the $Mg_{17}Al_{12}$ and Mg_2Sn precipitates show a pinning effect on the static recrystallized grains. Thus, after aging, the grain size of the as-extruded ATZ632 alloy decreases from 15.49 to 10.03 μm.

Figure 11 shows both the PF and IPF of SR grains and un-SR grains. The recrystallized grains account for ~20.49% of the full map (Figs. 11(a) and (b)). The peak component of the SR grains slightly shifts from the TD by ~10° owing to aging. In the corresponding IPF (Fig. 11(c)), the high-intensity component is distributed at the $\langle 10\bar{1}4 \rangle$ pole along the TD, thus forming a sector area centered at the $\langle 10\bar{1}3 \rangle$ pole. In the RD, no high-intensity distribution is observed and the intensity is uniformly distributed along $\langle 10\bar{1}0 \rangle$ to $\langle 11\bar{2}0 \rangle$ and $\langle 0001 \rangle$. The c-axis of the SR grain crystal is almost perpendicular to the ED, which increases the intensity of the (0001) basal texture. The PF of un-SR (Fig. 11(e)) shows two high-intensity textural components compared with the PF of SR. Based on the IPF (Fig. 11(f)) of un-SR grains, the peak intensity along the TD is distributed at the $\langle 0001 \rangle$ pole and the peak intensity along the RD is distributed at the $\langle 11\bar{2}0 \rangle$ pole. These results show that the volume fraction of the SR grains increases with a preferential grain growth ($\langle 0001 \rangle \perp$ ED) during aging. Moreover, compared with the as-extruded sample (Fig. 3(c)), the c-axis of the nonrecrystallized grains tends to be oriented parallel to the ED with an increase in aging duration. The volume fraction of the grains around the $\langle 11\bar{2}0 \rangle$ pole along the RD is 14.19% of the full map. The area of the un-SR grains with large sizes ($\langle 11\bar{2}0 \rangle$//RD) accounts for 14.19%, which is larger than that of the SR grains (8.66%). Therefore, the
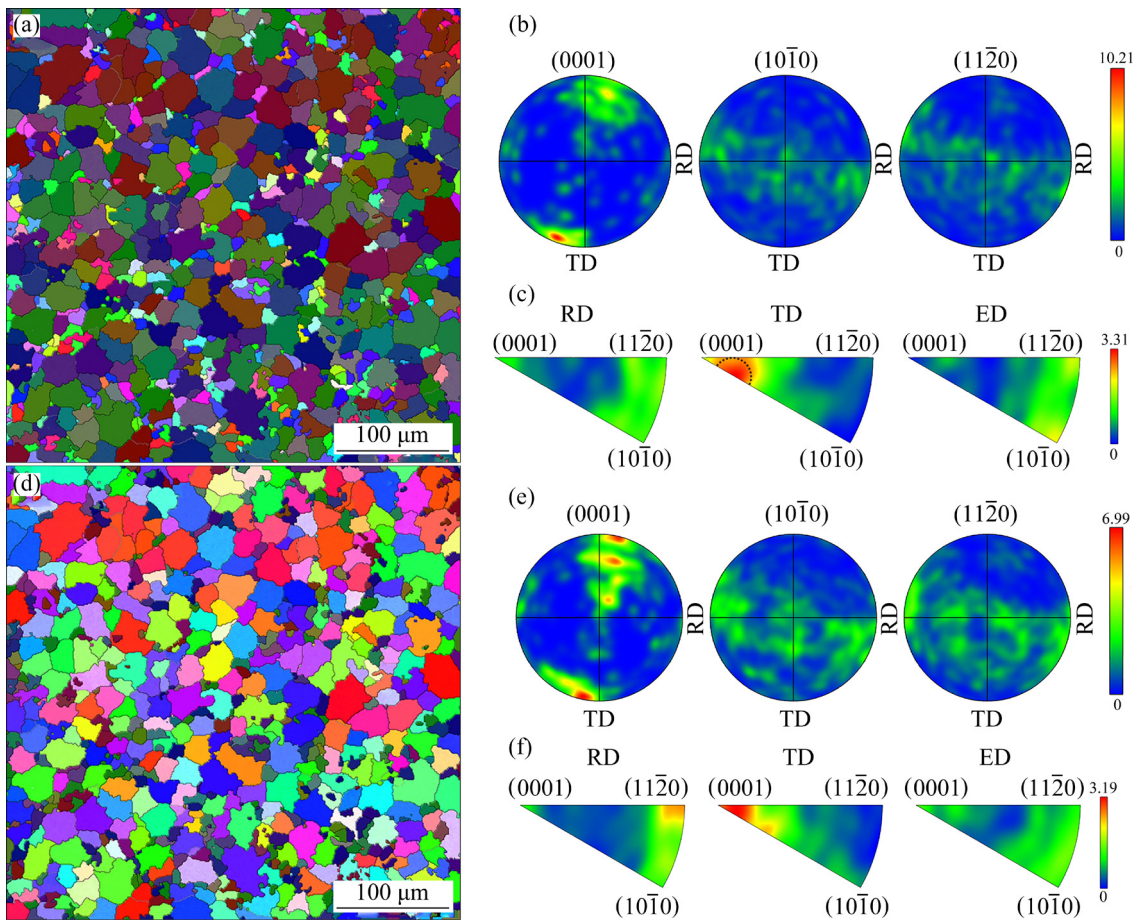
Fig. 11 Inverse pole and pole figures of SR area (a−c), and inverse pole and pole figures of un-SR area (d−f)

basal texture weakens after aging and the grain growth during aging may strengthen the basal fiber texture [27] or the rotation of the recrystallized grains [28,29]. LIU et al [30] reported the high boundary migration ability of the $\langle 0001 \rangle$//ED components and the consumption of $\langle 0001 \rangle \perp$ED grains by the $\langle 0001 \rangle$//ED grains with an increase in the grain growth. Herein, the aging temperature of 150 °C is lower than other reported temperatures in Refs. [31−33] and the related mechanism must be investigated in the future.

$Mg_{17}Al_{12}$ precipitates from the supersaturated matrix after aging; moreover, the precipitates grow along the basal plane. The (0001) basal plane is the primary slip plane of the Mg alloy; furthermore, the continuous $Mg_{17}Al_{12}$ precipitates could not pin the dislocation movement. Thus, after aging, the $Mg_{17}Al_{12}$ precipitates show a slight effect on the improvement of the YS of the as-extruded ATZ632 alloy. The Mg_2Sn phase in the as-extruded alloy can promote the precipitation of the Mg−Zn phase [34], leading to the precipitation of Mg_4Zn_7 after aging. JUNG et al [35] reported that when the Zn content

was 2 wt.%, the dispersion strengthening exerted no effect on the strength improvement. The precipitation of the Mg_4Zn_7 phase along the prismatic plane can limit the basal-plane slip, which can limit the movement of dislocations to increase the YS.

4.2 Influence of aging on mechanical properties

The strength of the Mg alloy is influenced by certain factors. The increase in the volume fraction of $Mg_{17}Al_{12}$ and Mg_4Zn_7 precipitates contributes to the precipitation strengthening [36]. Mg_4Zn_7 perpendicular to the basal plane can limit the sliding of dislocations on the basal plane, improving the alloy strength. Moreover, the Mg_2Sn phase does not show new precipitates during aging; hence, only the contribution of $Mg_{17}Al_{12}$ and Mg_4Zn_7 is considered to increase the YS. The basal and prismatic precipitates exert different hindering effects compared to the basal slip. The increment in YS ($\Delta\sigma$) is related to the hardening of the basal slip. The general formula for calculating $\Delta\sigma$ is listed below:

$$\Delta\sigma = \frac{Gb}{2\pi\lambda\sqrt{1-v}}\ln\frac{d_p}{r_0} \tag{1}$$

where G denotes the shear modulus of the Mg matrix, b represents the magnitude of the Burgers vector for the gliding dislocations, λ represents the effective planar interparticle spacing on the slip plane, v represents the Poisson ratio of the Mg matrix, d_p represents the mean planar diameter of the particles along the slip plane, and r_0 is the core radius of the dislocations; for magnesium basal surface, $r_0=b$ [37].

Based on Eq. (1), NIE [38] derived two equations. The equation for strengthening the lamellar precipitation on the basal plane is expressed as follows:

$$\Delta\sigma = \frac{Gb}{2\pi\sqrt{1-v\left(\frac{0.953}{\sqrt{f}}-1\right)D}}\ln\frac{D}{b} \tag{2}$$

where f represents the volume fraction of the precipitates, and D represents the average diameter of the precipitates.

The equation for strengthening the lamellar precipitation on the prismatic plane is expressed as follows:

$$\Delta\sigma = Gb/\left[2\pi\sqrt{1-v}(0.825\sqrt{\frac{DT}{f}}-0.393D-\right.$$
$$\left.0.886T)\right]\ln\frac{0.886\sqrt{DT}}{b} \tag{3}$$

where T represents the average thickness of the precipitates. Based on the TEM images, the D, T, and f values of the $Mg_{17}Al_{12}$ and Mg_4Zn_7 phases are shown in Table 2.

Table 2 D, T, and f values

Phase	D/nm	T/nm	f/%
$Mg_{17}Al_{12}$	86.77	37	2.85
Mg_4Zn_7	613.85	30	7.16

Fine-grain strengthening is a common method for improving the mechanical properties of Mg alloys [39]. Using the Hall–Petch equation:

$$\sigma_{gb}=kd^{-1/2} \tag{4}$$

where σ_{gb} is the strength induced by grain boundaries, k denotes the Hall–Petch coefficient

(320 MPa·μm$^{1/2}$) [40], and d represents the average grain size. The YS increases as the grain size decreases. After aging, the effect of grain refinement on the alloy strength can be estimated using the following equation:

$$\Delta\sigma_{gb}=k(d_{\text{peak-aged}}^{-1/2}-d_{\text{as-extruded}}^{-1/2}) \tag{5}$$

For the Mg alloy, the G and v values are 16.5 GPa and 0.35, respectively. Using Eqs. (3) and (4), $\Delta\sigma_{Mg_4Zn_7}=14.103$ MPa and $\Delta\sigma_{Mg_{17}Zn_{12}}=7.483$ MPa.

Based on the calculation results of Eq. (5), the contribution of grain refinement to the alloy strength is 18.402 MPa.

Furthermore, the texture influences the alloy strength based on its effect on the Hall–Petch constants [41]. The general formula for calculating σ_0 is listed below:

$$\sigma_0=m\tau_0 \tag{6}$$

where τ_0 is the single-crystal resolved stress, and m is the Taylor orientation factor, which is related to the basal texture of the material. In randomly oriented HCP polycrystals (without a texture), m is ~6.5. Generally, the m value is calculated to be 6.5 times the textural strength. For the as-extruded and as-aged alloys, the m values are 63.63 and 45.175, respectively. Based on a previous report [42], the τ_0 of the basal slip of Mg is 0.6 MPa. Therefore, the relative contribution from textural strengthening is approximately −11.073 MPa.

Finally, the aging treatment performed after extrusion often loads to a change in the dislocation density inside the alloy [43]. Moreover, the average full width at the half maximum value of the XRD changes considerably after the alloy aging treatment, i.e., from 0.375 to 0.248. This shows that the dislocation density of the alloy has changed substantially. Dislocation–dislocation interactions increase the yield stress according to the following relation:

$$\Delta\sigma_\rho=M\alpha Gb\rho^{1/2} \tag{7}$$

where $\Delta\sigma_\rho$ denotes the strength contribution from dislocation–dislocation interactions, M denotes the Taylor factor (6.5 for Mg [44]), α is a constant (usually 0.33 [45]), G for Mg is 16.6 GPa at room temperature [46], b for the basal slip in Mg is 0.321 nm, and ρ represents the dislocation density, which can be calculated using the Dunn formula:

$$\rho = \frac{L^2}{4.35b^2} \qquad (8)$$

where L is the full width at half maximum value. Combining Eqs. (7) and (8), the contribution of the dislocation strengthening to the alloy strength is -2.168 MPa.

Combining the abovementioned calculations, the total $\Delta\sigma = \Delta\sigma_{gb} + \Delta\sigma_{Mg_4Zn_7} + \Delta\sigma_{Mg_{17}Al_{12}} + \Delta\sigma_0 + \Delta\sigma_\rho = 26.747$ MPa. Based on these calculation results, the precipitation of the Mg_4Zn_7 phase after aging improves the alloy strength ($\sim$39.6% increase in intensity).

With the weakening of the alloy texture after aging, additional slip systems can be activated to coordinate the deformation, increasing the EL [47,48]. However, the EL of the ATZ632 alloy decreases after aging. High-density precipitation, distributed along the grain boundary after aging, causes the accumulation of dislocations close to the grain boundary, increasing the stress accumulation and decreasing the EL of the ATZ632 alloy after aging [49]. Furthermore, aging depletes the solute element and deactivates the solution softening of the prismatic slip, playing a role in accommodating local deformation incompatibility [50]. Moreover, the consumption of solute elements and the formation of precipitates cause reduction in the EL.

5 Conclusions

(1) For the as-extruded ATZ632 alloy, the amount of $Mg_{17}Al_{12}$ phase increased and Mg_4Zn_7 phase precipitated after aging. The YS and UTS of the peak-aged ATZ632 alloy reached 252.5 and 416.2 MPa, respectively.

(2) In the ATZ632 alloy, after peak aging, multiple lamellar $Mg_{17}Al_{12}$ phases precipitated and grew parallel to the basal plane of the matrix; furthermore, the rod-like Mg_4Zn_7 phase grew perpendicularly to the basal plane. Because of the rotation of some part of the un-SR grains, the pyramidal plane was parallel to the RD, weakening the basal texture.

(3) Mg_4Zn_7 precipitation after aging increased the YS, and the $Mg_{17}Al_{12}$ phase and fine-grained strengthening also increased certain intensity.

References

[1] TESAR K, BALIK K, SUCHARDA Z. Direct extrusion of thin Mg wires for biomedical applications [J]. Transactions of Nonferrous Metals Society of China, 2020, 30: 373−381.

[2] ZHAO D X, MA X L, SRIVASTAVA A, TURNER G, KARAMAN I, XIE K Y. Significant disparity of non-basal dislocation activities in hot-rolled highly-textured Mg and Mg−3Al−1Zn alloy under tension [J]. Acta Materialia, 2021, 207: 116691.

[3] ZHONG L P, WANG Y J. Microstructure evolution and optimum parameters analysis for hot working of new type Mg−8Sn−2Zn−0.5Cu alloy [J]. Transactions of Nonferrous Metals Society of China, 2019, 29: 2290−2299.

[4] PENG P, ZHANG K M, SHE J, TANG A T, ZHANG J Y, SONG K, YANG Q S, PAN F S. Role of second phases and grain boundaries on dynamic recrystallization behavior in ZK60 magnesium alloy [J]. Journal of Alloys and Compounds, 2021, 861: 157958.

[5] SUN J P, LI B J, YUAN J, LI X K, XU B Q, YANG Z Q, HAN J, JIANG J H, WU G S, MA A B. Developing a high-performance Mg−5.7Gd−1.9Ag wrought alloy via hot rolling and aging [J]. Materials Science and Engineering: A, 2021, 803: 140707.

[6] SUN Y D, LI W, SHI X F, TIAN L. A uniformly fine-grained Mg−Y−Nd−Zr magnesium alloy with simultaneously optimized strength and ductility processed by forging and ECAP [J]. Materials Research Express, 2020, 7: 116520.

[7] JIANG B, DONG Z H, ZHANG A, SONG J F, PAN F S. Recent advances in micro-alloyed wrought magnesium alloys: Theory and design [J]. Transactions of Nonferrous Metals Society of China, 2022, 32: 1741−1780.

[8] LI Z, PENG Z Y, QIU Y B, QI K, CHEN Z Y, GUO X P. Study on heat treatment to improve the microstructure and corrosion behavior of ZK60 magnesium alloy [J]. Journal of Materials Research and Technology, 2020, 9: 11201−11219.

[9] SONG B, DU Z W, YANG Q S. Effect of pre-rolling path on mechanical properties of rolled ZK60 alloys [J]. Transactions of Nonferrous Metals Society of China, 2021, 31: 1322−1338.

[10] LV B J, WANG S, CUI N, GUO F. Twinning and dynamic recrystallization of Mg−7Sn−3Zn alloy under high strain rate hot compression [J]. Materials Science and Engineering: A, 2021, 809: 140986.

[11] HU H J, ZHANG D F, YANG M B, DENG M. Grain refinement in AZ31 magnesium alloy rod fabricated by extrusion-shearing severe plastic deformation process [J]. Transactions of Nonferrous Metals Society of China, 2011, 21: 243−249.

[12] LI L H, CAO H S, QI F G, WANG Q, ZHAO N, LIU Y D, YE X, OUYANG X P. Effect of heat treatment on microstructure and mechanical properties of Mg−5Zn−1Mn alloy tube [J]. Metals, 2020, 10(3): 301.

[13] JUNG I C, KIM Y K, CHO T H, OH S H, KIM T E, SHON S W, KIM W T, KIM D H. Suppression of discontinuous precipitation in AZ91 by addition of Sn [J]. Metals and Materials International, 2014, 20: 99−103.

[14] LI R G, XU Y, QI W, AN J, LU Y, CAO Z Y, LIU Y B. Effect of Sn on the microstructure and compressive deformation behavior of the AZ91D aging alloy [J]. Materials Characterization, 2008, 59: 1643−1649.

[15] WU H Y, ZHANG D F, JIANG L Y, FENG J K, ZHAO Y, PAN F S. Effects of Zn addition on microstructure and mechanical properties of Mg−8Al−2Sn alloy [J]. Rare Metal Materials and Engineering, 2019, 48: 2091−2098.

[16] SHI Z Z, ZHANG W Z, GU X F. Characterization and interpretation of the morphology of a Mg₂Sn precipitate with irrational facets in a Mg–Sn–Mn alloy [J]. Philosophical Magazine, 2012, 92: 1071−1082.

[17] WANG B, PAN F S, CHEN X H, GUO W, MAO J J. Microstructure and mechanical properties of as-extruded and as-aged Mg−Zn−Al−Sn alloys [J]. Materials Science and Engineering: A, 2016, 656: 165−173.

[18] MENDIS C L, BETTLES C J, GIBSON M A, HUTCHINSON C R. An enhanced age hardening response in Mg−Sn based alloys containing Zn [J]. Materials Science and Engineering: A, 2006, 435/436: 163−171.

[19] SASAKI T T, OH-ISHI K, OHKUBO T, HONO K. Effect of double aging and microalloying on the age hardening behavior of a Mg−Sn−Zn alloy [J]. Materials Science and Engineering: A, 2011, 530: 1−8.

[20] LIU F Y, XIN R L, ZHANG M X, PÉREZ-PRADO M T, LIU Q. Evaluating the orientation relationship of prismatic precipitates generated by detwinning in Mg alloys [J]. Acta Materialia, 2020, 195: 263−273.

[21] GAO X, NIE J F. Characterization of strengthening precipitate phases in a Mg−Zn alloy [J]. Scripta Materialia, 2007, 56: 645−648.

[22] CATORCENO L L C, de ABREU H F G D, PADILHA A F. Effects of cold and warm cross-rolling on microstructure and texture evolution of AZ31B magnesium alloy sheet [J]. Journal of Magnesium and Alloys, 2018, 6: 121−133.

[23] SHENG L Y, DU B N, HU Z Y, QIAO Y X, XIAO Z P, WANG B J, XU D K, ZHENG Y F, XI T F. Effects of annealing treatment on microstructure and tensile behavior of the Mg−Zn−Y−Nd alloy [J]. Journal of Magnesium and Alloys, 2020, 8: 601−613.

[24] GUAN D K, RAINFORTH W M, GAO J H, SHARP J, WYNNE B, MA L. Individual effect of recrystallisation nucleation sites on texture weakening in a magnesium alloy: Part 1— Double twins [J]. Acta Materialia, 2017, 135: 14−24.

[25] HUANG X, SUZUKI K, CHINO Y. Static recrystallization behavior of hot-rolled Mg−Zn−Ce magnesium alloy sheet [J]. Journal of Alloys and Compounds, 2017, 724: 981−990.

[26] SHI J J, CUI K X, WANG B S, DENG L, WANG C, XU Z R, LI Q. Effect of initial microstructure on static recrystallization of Mg−3Al−1Zn alloy [J]. Materials Characterization, 2017, 129: 104−113.

[27] HANTZSCHE K, BOHLEN J, WENDT J, KAINER K U, YI S B, LETZIG D. Effect of rare earth additions on microstructure and texture development of magnesium alloy sheets [J]. Scripta Materialia, 2010, 63: 725−730.

[28] WANG Y J, ZHONG L P, DOU Y C, ZHANG X F. Revealing grain structure development and texture evolution during elastic stress-assist aging of Mg−Zn alloys [J]. Journal of Alloys and Compounds, 2021, 881: 160474.

[29] WANG Q H, BIN J, AITAO T, JIE F, JIANG Z T. Unveiling annealing texture formation and static recrystallization kinetics of hot-rolled Mg−Al−Zn−Mn−Ca alloy [J]. Journal of Materials Science & Technology, 2020, 43: 104−118.

[30] LIU L, ZHOU X J, YU S L, ZHANG J, LU X Z, SHU X, SU Z J. Effects of heat treatment on mechanical properties of an extruded Mg−4.3Gd−3.2Y−1.2Zn−0.5Zr alloy and establishment of its Hall−Petch relation [J]. Journal of Magnesium and Alloys, 2022, 10: 501−512.

[31] LEE S W, HAN G, JUN T S, PARK S H. Effects of initial texture on deformation behavior during cold rolling and static recrystallization during subsequent annealing of AZ31 alloy [J]. Journal of Materials Science & Technology, 2021, 66: 139−149.

[32] YAO Y, LIU C M, GAO Y H, YU S L, JIANG S N, CHEN Z X. Annealing-induced microstructural evolution and mechanical anisotropy improvement of the Mg−Gd−Y−Zr alloy processed by hot ring rolling [J]. Materials Characterization, 2018, 144: 641−651.

[33] ZHAO L Y, YAN H, CHEN R S, HAN E H. Quasi-in-situ observations of low-angle grain boundaries, twins and texture evolution during continuous annealing in a cold-rolled Mg−Zn−Gd alloy [J]. Materials Characterization, 2020, 170: 110697.

[34] CHEN J H, CHEN Z H, YAN H G, ZHANG F Q, LIAO K. Effects of Sn addition on microstructure and mechanical properties of Mg−Zn−Al alloys [J]. Journal of Alloys and Compounds, 2008, 461: 209−215.

[35] JUNG J G, PARK S H, YU H, KIM Y M, LEE Y K, YOU B S. Improved mechanical properties of Mg−7.6Al−0.4Zn alloy through aging prior to extrusion [J]. Scripta Materialia, 2014, 93: 8−11.

[36] ZHANG Ju-mei, WANG Zhi-fu, JIANG Bai-ling. Effects of T6 treatment on precipitation of β-Mg₁₇Al₁₂ phase and fracture properties of AZ91 alloy [J]. Hot Working Technology, 2011, 40: 153−156.

[37] HIDALGO-MANRIQUE P, ROBSON J D, PÉREZ-PRADO M T. Precipitation strengthening and reversed yield stress asymmetry in Mg alloys containing rare-earth elements: A quantitative study [J]. Acta Materialia, 2017, 124: 456−467.

[38] NIE J F. Effects of precipitate shape and orientation on dispersion strengthening in magnesium alloys [J]. Scripta Materialia, 2003, 48: 1009−1015.

[39] WEI K, HU R, YIN D D, XIAO L R, PANG S, CAO Y, ZHOU H, ZHAO Y H, ZHU Y T. Grain size effect on tensile properties and slip systems of pure magnesium [J]. Acta Materialia, 2021, 206: 116604.

[40] CHENG W L, TIAN Q W, YU H, ZHANG H, YOU B S. Strengthening mechanisms of indirect-extruded Mg−Sn based alloys at room temperature [J]. Journal of Magnesium and Alloys, 2014, 2: 299−304.

[41] RAO G S, PRASAD Y V R K. Grain boundary strengthening in strongly textured magnesium produced by hot rolling [J].

Metallurgical Transactions A, 1982, 13: 2219−2226.

[42] MALDAR A, WANG L Y, ZHU G M, ZENG X Q. Investigation of the alloying effect on deformation behavior in Mg by visco-plastic self-consistent modeling [J]. Journal of Magnesium and Alloys, 2020, 8: 210−218.

[43] KANG Y H, WANG X X, ZHANG N, YAN H, CHEN R S. Effect of pre-deformation on microstructure and mechanical properties of WE43 magnesium alloy [J]. Materials Science and Engineering: A, 2017, 689: 435−445.

[44] CABIBBO M, SPIGARELLI S. A TEM quantitative evaluation of strengthening in an Mg–RE alloy reinforced with SiC [J]. Materials Characterization, 2011, 62: 959−969.

[45] STARINK M J, QIAO X G, ZHANG J W, GAO N. Predicting grain refinement by cold severe plastic deformation in alloys using volume averaged dislocation generation [J]. Acta Materialia, 2009, 57: 5796−5811.

[46] NAGHDI F, MAHMUDI R, KANG J Y, KIM H S.

Contributions of different strengthening mechanisms to the shear strength of an extruded Mg−4Zn−0.5Ca alloy [J]. Philosophical Magazine, 2015, 95: 3452−3466.

[47] LI J L, WU D, CHEN R S, HAN E H. Anomalous effects of strain rate on the room-temperature ductility of a cast Mg−Gd−Y−Zr alloy [J]. Acta Materialia, 2018, 159: 31−45.

[48] LV B J, WANG S, XU T W, GUO F. Effects of minor Nd and Er additions on the precipitation evolution and dynamic recrystallization behavior of Mg−6.0Zn−0.5Mn alloy [J]. Journal of Magnesium and Alloys, 2021, 9: 840−852.

[49] ZHAO X, GAO P C, ZHANG Z M, WANG Q, YAN F F. Fatigue characteristics of the extruded AZ80 automotive wheel [J]. International Journal of Fatigue, 2020, 132: 105393.

[50] ZHANG J, DOU Y C, LIU G B, GUO Z X. First-principles study of stacking fault energies in Mg-based binary alloys [J]. Computational Materials Science, 2013, 79: 564−569.

挤压态和峰值时效态 Mg−6Al−3Sn−2Zn 合金
显微组织与力学性能之间的关系

王 森，吕滨江，徐铁伟，崔 宁，郭 峰

青岛理工大学 机械与汽车工程学院，青岛 266525

摘 要：研究挤压态和时效态 Mg−6Al−3Sn−2Zn (ATZ632)合金的显微组织和力学性能。挤压态 ATZ632 合金表现出优异的力学性能，其屈服强度 (YS)、极限抗拉强度 (UTS) 和伸长率 (EL) 分别为 216.4 MPa、344.3 MPa 和 18.4%。经时效处理后，$Mg_{17}Al_{12}$ 析出相体积分数增加且出现 Mg_4Zn_7 相，$Mg_{17}Al_{12}$ 相平行于基面，Mg_4Zn_7 垂直于 α-Mg 的(0001)面析出，从而使时效态 ATZ632 合金的 YS 和 UTS 分别增加到 252.5 和 416.2 MPa；但 EL 下降至 10.1%。经过 150 ℃较低温度时效处理后，合金中出现静态再结晶晶粒，且静态再结晶晶粒的 c 轴垂直于挤压方向，其取向呈高度一致性。

关键词：显微组织；力学性能；时效；强化机制；静态再结晶

(Edited by Wei-ping CHEN)